REPORT DOCUMENTATION PAGE

Form Approved OMB NO. 0704-0188

1. REPORT DATE (DD-MM-YYYY)	2. REPORT TYPE New Reprint	3. DATES COVERED (From - To) -

4. TITLE AND SUBTITLE	5a. CONTRACT NUMBER
Temperature dependent spectral response and detectivity of GeSn photoconductors on silicon for short wave infrared detection	W911NF-13-1-0196
	5b. GRANT NUMBER
	5c. PROGRAM ELEMENT NUMBER

6. AUTHORS	5d. PROJECT NUMBER
Benjamin R. Conley, Aboozar Mosleh, Seyed Amir Ghetmiri, Wei Du, Richard A. Soref, Greg Sun, Joe Margetis, John Tolle, Hameed A. Naseem, Shui-Qing Yu	
	5e. TASK NUMBER
	5f. WORK UNIT NUMBER

7. PERFORMING ORGANIZATION NAMES AND ADDRESSES	8. PERFORMING ORGANIZATION REPORT NUMBER
University of Arkansas 210 Administration Building 1 University of Arkansas Fayetteville, AR 72701 -1201	

9. SPONSORING/MONITORING AGENCY NAME(S) AND ADDRESS (ES)	10. SPONSOR/MONITOR'S ACRONYM(S) ARO
U.S. Army Research Office P.O. Box 12211 Research Triangle Park, NC 27709-2211	11. SPONSOR/MONITOR'S REPORT NUMBER(S) 64461-EL-DRP.2

12. DISTRIBUTION AVAILIBILITY STATEMENT

Approved for public release; distribution is unlimited.

13. SUPPLEMENTARY NOTES
The views, opinions and/or findings contained in this report are those of the author(s) and should not contrued as an official Department of the Army position, policy or decision, unless so designated by other documentation.

14. ABSTRACT

The GeSn direct gap material system, with Si complementary-metal-oxide semiconductor (CMOS) compatibility, presents a promising solution for direct incorporation of focal plane arrays with short wave infrared detection on Si. A temperature dependence study of GeSn photoconductors with 0.9, 3.2, and 7.0 % Sn was conducted using both electrical and optical characterizations from 300 to 77 K. The GeSn layers were grown on Si substrates using a commercially available chemical vapor deposition reactor in a Si CMOS compatible process. Carrier activation energies due to ionization and trap states are extracted from the temperature dependent dark I-V characteristics. The

15. SUBJECT TERMS
Si Photonics, GeSn, infrared Detection, Photoconductor

16. SECURITY CLASSIFICATION OF:			17. LIMITATION OF ABSTRACT	15. NUMBER OF PAGES	19a. NAME OF RESPONSIBLE PERSON Shui-Qing (Fisher) Yu
a. REPORT UU	b. ABSTRACT UU	c. THIS PAGE UU	UU		19b. TELEPHONE NUMBER 479-575-7265

Report Title

Temperature dependent spectral response and detectivity of GeSn photoconductors on silicon for short wave infrared detection

ABSTRACT

The GeSn direct gap material system, with Si complementary-metal-oxide semiconductor (CMOS) compatibility, presents a promising solution for direct incorporation of focal plane arrays with short wave infrared detection on Si. A temperature dependence study of GeSn photoconductors with 0.9, 3.2, and 7.0 % Sn was conducted using both electrical and optical characterizations from 300 to 77 K. The GeSn layers were grown on Si substrates using a commercially available chemical vapor deposition reactor in a Si CMOS compatible process. Carrier activation energies due to ionization and trap states are extracted from the temperature dependent dark I-V characteristics. The temperature dependent spectral response of each photoconductor was measured, and a maximum long wavelength response to 2.1 ?m was observed for the 7.0 % Sn sample. The DC responsivity measured at 1.55 ?m showed around two orders of magnitude improvement at reduced temperatures for all samples compared to room temperature measurements. The noise current and temperature dependent specific detectivity (D*) were also measured for each sample at 1.55 ?m, and a maximum D* value of 1×10^9 cm·?Hz/W was observed at 77 K.

REPORT DOCUMENTATION PAGE (SF298)
(Continuation Sheet)

Continuation for Block 13

ARO Report Number   64461.2-EL-DRP
Temperature dependent spectral response and ...

Block 13: Supplementary Note

Temperature dependent spectral response and detectivity of GeSn photoconductors on silicon for short wave infrared detection

Benjamin R. Conley,[1,*] **Aboozar Mosleh,**[1] **Seyed Amir Ghetmiri,**[1] **Wei Du,**[1] **Richard A. Soref,**[2] **Greg Sun,**[2] **Joe Margetis,**[3] **John Tolle,**[3] **Hameed A. Naseem,**[1] **and Shui-Qing Yu**[1]

[1]*Department of Electrical Engineering, University of Arkansas, Fayetteville, AR 72701, USA*
[2]*Department of Physics, University of Massachusetts Boston, Boston, MA 02125, USA*
[3]*ASM, Phoenix, AZ 85034, USA*
[*]brconley@uark.edu

Abstract: The GeSn direct gap material system, with Si complementary-metal-oxide semiconductor (CMOS) compatibility, presents a promising solution for direct incorporation of focal plane arrays with short wave infrared detection on Si. A temperature dependence study of GeSn photoconductors with 0.9, 3.2, and 7.0 % Sn was conducted using both electrical and optical characterizations from 300 to 77 K. The GeSn layers were grown on Si substrates using a commercially available chemical vapor deposition reactor in a Si CMOS compatible process. Carrier activation energies due to ionization and trap states are extracted from the temperature dependent dark I-V characteristics. The temperature dependent spectral response of each photoconductor was measured, and a maximum long wavelength response to 2.1 μm was observed for the 7.0 % Sn sample. The DC responsivity measured at 1.55 μm showed around two orders of magnitude improvement at reduced temperatures for all samples compared to room temperature measurements. The noise current and temperature dependent specific detectivity (D^*) were also measured for each sample at 1.55 μm, and a maximum D^* value of 1×10^9 cm·√Hz/W was observed at 77 K.

References and links

1. A. Rogalski, "Progress in focal plane array technologies," Progress in Quantum Electronics **36**, 342-473 (2012).
2. A. Rogalski and R. Ciupa, "Performance limitation of short wavelength infrared InGaAs and HgCdTe photodiodes," in *1998 U S Workshop on the Physics and Chemistry of II-VI Materials*, J. Electron. Mater. 1998), 630-636.
3. G. Roelkens, J. Van Campenhout, J. Brouckaert, D. Van Thourhout, R. Baets, P. R. Romeo, P. Regreny, A. Kazmierczak, C. Seassal, X. Letartre, G. Hollinger, J. M. Fedeli, L. Di Cioccio, and C. Lagahe-Blanchard, "III-V/Si photonics by die-to-wafer bonding," Materials Today **10**, 36-43 (2007).
4. K. Akahane, N. Yamamoto, S.-i. Gozu, and N. Ohtani, "Heteroepitaxial growth of GaSb on Si(001) substrates," J. of Crys. Growth **264**, 21-25 (2004).
5. B. Kunert, S. Zinnkann, K. Volz, and W. Stolz, "Monolithic integration of Ga(NAsP)/(BGa)P multi-quantum well structures on (0 0 1) silicon substrate by MOVPE," Journal of Crystal Growth **310**, 4776-4779 (2008).
6. T. Wang, H. Liu, A. Lee, F. Pozzi, and A. Seeds, "1.3-μm InAs/GaAs quantum-dot lasers monolithically grown on Si substrates," Opt. Express **19**, 11381-11386 (2011).
7. M. Bauer, J. Taraci, J. Tolle, A. V. G. Chizmeshya, S. Zollner, D. J. Smith, J. Menendez, C. Hu, and J. Kouvetakis, "Ge–Sn semiconductors for band-gap and lattice engineering," Appl. Phys. Lett. **81**, 2992 (2002).

8. R. A. Soref, "Silicon-based optoelectronics," Proceedings of the IEEE **81**, 1687-1706 (1993).

9. V. D'Costa, C. Cook, A. Birdwell, C. Littler, M. Canonico, S. Zollner, J. Kouvetakis, and J. Menéndez, "Optical critical points of thin-film $Ge_{1-y}Sn_y$ alloys: A comparative $Ge_{1-y}Sn_y/Ge_{1-x}Si_x$ study," Phys. Rev. B **73**(2006).

10. R. Chen, H. Lin, Y. Huo, C. Hitzman, T. I. Kamins, and J. S. Harris, "Increased photoluminescence of strain-reduced, high-Sn composition $Ge_{1-x}Sn_x$ alloys grown by molecular beam epitaxy," Appl. Phys. Lett. **99**, 181125 (2011).

11. G. Grzybowski, R. T. Beeler, L. Jiang, D. J. Smith, J. Kouvetakis, and J. Menendez, "Next generation of $Ge_{1-y}Sn_y$ (y = 0.01-0.09) alloys grown on Si(100) via Ge_3H_8 and SnD_4: Reaction kinetics and tunable emission," Appl. Phys. Lett. **101**, 072105 (2012).

12. S. Wirths, D. Buca, G. Mussler, A. T. Tiedemann, B. Holländer, P. Bernardy, T. Stoica, D. Grützmacher, and S. Mantl, "Reduced Pressure CVD Growth of Ge and $Ge_{1-x}Sn_x$ Alloys," ECS J. of Solid State Sci. and Technol. **2**, 99-102 (2013).

13. F. Gencarelli, B. Vincent, J. Demeulemeester, A. Vantomme, A. Moussa, A. Franquet, A. Kumar, H. Bender, J. Meersschaut, W. Vandervorst, R. Loo, M. Caymax, K. Temst, and M. Heyns, "Crystalline Properties and Strain Relaxation Mechanism of CVD Grown GeSn," ECS J. of Solid State Sci. and Technol. **2**, 134-137 (2013).

14. B. Vincent, F. Gencarelli, H. Bender, C. Merckling, B. Douhard, D. H. Petersen, O. Hansen, H. H. Henrichsen, J. Meersschaut, W. Vandervorst, M. Heyns, R. Loo, and M. Caymax, "Undoped and in-situ B doped GeSn epitaxial growth on Ge by atmospheric pressure-chemical vapor deposition," Appl. Phys. Lett. **99**, 152103 (2011).

15. A. Mosleh, S. Ghetmiri, B. Conley, M. Hawkridge, M. Benamara, A. Nazzal, J. Tolle, S.-Q. Yu, and H. Naseem, "Material Characterization of $Ge_{1-x}Sn_x$ Alloys Grown by a Commercial CVD System for Optoelectronic Device Applications," J. Electron. Mater. **43**, 938-946 (2014).

16. S. Kim, J. Gupta, N. Bhargava, M. Coppinger, and J. Kolodzey, "Current--Voltage Characteristics of GeSn/Ge Heterojunction Diodes Grown by Molecular Beam Epitaxy," Electron Device Lett., IEEE **34**, 1217-1219 (2013).

17. R. Cheng, W. Wang, X. Gong, L. Sun, P. Guo, H. Hu, Z. Shen, G. Han, and Y.-C. Yeo, "Relaxed and Strained Patterned Germanium-Tin Structures: A Raman Scattering Study," ECS J. of Solid State Sci. and Technol. **2**, 138-145 (2013).

18. H. H. Tseng, K. Y. Wu, H. Li, V. Mashanov, H. H. Cheng, G. Sun, and R. A. Soref, "Mid-infrared electroluminescence from a $Ge/Ge_{0.922}Sn_{0.078}/Ge$ double heterostructure p-i-n diode on a Si substrate," Appl. Phys. Lett. **102**, 182106 (2013).

19. R. Roucka, J. Mathews, C. Weng, R. Beeler, J. Tolle, J. Menendez, and J. Kouvetakis, "High-Performance Near-IR Photodiodes: A Novel Chemistry-Based Approach to Ge and Ge–Sn Devices Integrated on Silicon," Quantum Electronics, IEEE Journal of **47**, 213-222 (2011).

20. J. Kouvetakis, J. Mathews, R. Roucka, A. V. G. Chizmeshya, J. Tolle, and J. Menendez, "Practical Materials Chemistry Approaches for Tuning Optical and Structural Properties of Group IV Semiconductors and Prototype Photonic Devices," IEEE Photonics Journal (2010).

21. H. H. Tseng, H. Li, V. Mashanov, Y. J. Yang, H. H. Cheng, G. E. Chang, R. A. Soref, and G. Sun, "GeSn-based p-i-n photodiodes with strained active layer on a Si wafer," Appl. Phys. Lett. **103**, 231907 (2013).

22. M. Oehme, M. Schmid, M. Kaschel, M. Gollhofer, D. Widmann, E. Kasper, and J. Schulze, "GeSn p-i-n detectors integrated on Si with up to 4% Sn," Appl. Phys. Lett. **101**, 141110 (2012).

23. A. Gassenq, F. Gencarelli, J. Van Campenhout, Y. Shimura, R. Loo, G. Narcy, B. Vincent, and G. Roelkens, "GeSn/Ge heterostructure short-wave infrared photodetectors on silicon," Opt. Express **20**, 27297-27303 (2012).

24. M. Oehme, K. Kostecki, K. Ye, S. Bechler, K. Ulbricht, M. Schmid, M. Kaschel, M. Gollhofer, R. Körner, W. Zhang, E. Kasper, and J. Schulze, "GeSn-on-Si normal incidence photodetectors with bandwidths more than 40 GHz," Opt. Express **22**, 839-846 (2014).

25. M.-Y. Ryu, T. R. Harris, Y. K. Yeo, R. T. Beeler, and J. Kouvetakis, "Temperature-dependent photoluminescence of Ge/Si and $Ge_{1-y}Sn_y/Si$, indicating possible indirect-to-direct bandgap transition at lower Sn content," Applied Physics Letters **102**, 171908 (2013).

26. P. Moontragoon, R. A. Soref, and Z. Ikonic, "The direct and indirect bandgaps of unstrained $Si_xGe_{1-x-y}Sn_y$ and their photonic device applications," J. Appl. Phys. **112**, 073106 (2012).

27. J. M. Arias, J. G. Pasko, M. Zandian, S. H. Shin, G. M. Williams, L. O. Bubulac, R. E. DeWames, and W. E. Tennant, "Planar p-on-n HgCdTe heterostructure photovoltaic detectors," Applied Physics Letters **62**, 976-978 (1993).

28. H. Mohseni, A. Tahraoui, J. Wojkowski, M. Razeghi, G. J. Brown, W. C. Mitchel, and Y. S. Park, "Very long wavelength infrared type-II detectors operating at 80 K," Appl. Phys. Lett. **77**, 1572-1574 (2000).

29. J. D. Phillips, D. D. Edwall, and D. L. Lee, "Control of very-long-wavelength infrared HgCdTe detector-cutoff wavelength," Journal of Electronic Materials **31**, 664-668 (2002).

30. A. Rogalski, "Infrared detectors: status and trends," Progress in Quantum Electronics **27**, 59-210 (2003).

31. R. A. Street, K. W. Song, J. E. Northrup, and S. Cowan, "Photoconductivity measurements of the electronic structure of organic solar cells," Physical Review B **83**, 165207 (2011).
32. S. M. Sze and K. K. Ng, *Physics of Semiconductor Devices* (John Wiley & Sons, 2006).
33. M. Coppinger, J. Hart, N. Bhargava, S. Kim, and J. Kolodzey, "Photoconductivity of germanium tin alloys grown by molecular beam epitaxy," Applied Physics Letters **102**, - (2013).
34. Y. P. Varshni, "Temperature dependence of the energy gap in semiconductors," Physica **34**, 149-154 (1967).
35. S. L. Chuang, *Physics of photonic devices* (John Wiley & Sons, 2012), Vol. 80.
36. S. Nudelman, "The Detectivity of Infrared Photodetectors," Applied Optics **1**, 627-636 (1962).
37. V. Mitin, L. Reggiani, and L. Varani, "Generation-recombination noise in semiconductors," Noise and Fluctuations Control in Electronic Devices, 11-30 (2002).
38. S. L. Chuang, *Physics of photonic devices,* 2nd ed. (Wiley, 2009).
39. R. Roucka, S. Q. Yu, J. Tolle, Y. Y. Fang, S. N. Wu, J. Menendez, and J. Kouvetakis, "Photoresponse at 1.55 um in GeSn epitaxial films grown on Si," in *Lasers and Electro-Optics Society, 2007. LEOS 2007. The 20th Annual Meeting of the IEEE*, 2007), 178-179.
40. O. Nakatsuka, N. Tsutsui, Y. Shimura, S. Takeuchi, A. Sakai, and S. Zaima, "Mobility Behavior of Ge$_{1-x}$Sn$_x$ Layers Grown on Silicon-on-Insulator Substrates," Jpn. J. of Appl. Phys. **49**, 04DA10 (2010).
41. W.-S. Jung, J.-H. Park, A. Nainani, D. Nam, and K. C. Saraswat, "Fluorine passivation of vacancy defects in bulk germanium for Ge metal-oxide-semiconductor field-effect transistor application," Appl. Phys. Lett. **101**(2012).

1. Introduction

Detection of short wave infrared (SWIR) light with 2D focal plane arrays (FPA) is accomplished efficiently by only a few high cost semiconductor material alloys such as InGaAs or HgCdTe. These material systems have a high peak specific detectivity (D*) on the order of 10^{12} to 10^{13} cm·√Hz/W [1, 2], but cannot be produced on a cost efficient platform. The large scale processing of Si complementary metal-oxide-semiconductor (CMOS) devices would allow a CMOS compatible detector material to dramatically reduce the cost of SWIR based FPAs and increase the array size. Although progress has been made towards monolithic incorporation and bonding of the III-V materials on Si [3-6], the fundamental incorporation of those materials (In, Ga, Sb, and As) are difficult to grow monolithically on Si due to the large lattice mismatches. The pseudo-direct and tunable bandgap of Ge$_{1-x}$Sn$_x$, along with its CMOS compatibility have furthered the development of this material system for Si photonic applications [7, 8]. Incorporation of Sn reduces the difference between the indirect L-valley (0.67 eV) and direct Γ-valley (0.80 eV) in Ge. Early experimental results predicted this indirect-to-direct crossover point was around 11 % Sn [9], but more recent data suggests a relaxed Ge$_{1-x}$Sn$_x$ direct bandgap requires only 8 – 9 % Sn [10, 11]. Throughout the development of the Ge$_{1-x}$Sn$_x$ material system, the biggest challenge has been the stable incorporation of sufficient Sn needed for a room temperature direct bandgap material. Nevertheless, most of the growth related challenges have been mediated by non-equilibrium growth techniques on Si using commercially available chemical vapor deposition (CVD) reactors [12-15]. While Sn incorporation has also been demonstrated within molecular beam epitaxy (MBE) tools [16-18], the solid source deposition process is not as scalable for high yield manufacturing.

Further advancement of Ge$_{1-x}$Sn$_x$ technology has led to photodetectors that have already shown an extended long wavelength spectral response [19, 20] and a responsivity at 1.55 μm compared to Ge [21, 22]. Although those studies show promising advances in Ge$_{1-x}$Sn$_x$ fabrication and material quality, the temperature dependent spectral response of those devices were not investigated. Enhanced long wavelength spectral response out to 2.4 μm was, however, demonstrated for a photoconductor with 9 % Sn at room temperature using multiple quantum wells [23]. High speed operation of Ge$_{1-x}$Sn$_x$ based detectors has also been demonstrated up to 40 GHz opening up the possibility for high speed optical communication [24]. The high responsivity, long wavelength response, and high speed of those Ge$_{1-x}$Sn$_x$ detectors demonstrates the reliable fabrication methodology for this material system, and

establishes a cost effective long wavelength response on Si. However, to demonstrate this technology can be applicable for low cost, long wavelength focal plane arrays, a broader study of multiple Sn compositions and noise mechanisms is required. Thus, the next step in the development of $Ge_{1-x}Sn_x$ photodetectors is a systematic study of the temperature dependent characteristics and noise mechanisms specific to this material. The low temperature study is critical not only for the spectral response cut-off, but it also provides understanding of the defect mechanisms and activation energy related to this material. Other previous $Ge_{1-x}Sn_x$ photodiode and photoconductor studies have not systematically compared the performance metrics across different Sn compositions under the same size, temperature, and measurement conditions. In addition, carrier activation energy and noise baselines extracted from the temperature dependent measurements provide the design criteria needed for future detector applications. Thus far, the only temperature dependent study for the $Ge_{1-x}Sn_x$ material was conducted using photoluminescence on a sample with a low 0.3 % Sn composition [25]. Those optical measurements only provide fundamental information on the band structure, and do not give electrical transport and noise behavior characteristics needed to properly evaluate the detector figures of merit.

In this work, we report on the temperature dependent characterization of $Ge_{1-x}Sn_x$ photoconductors fabricated with 0.9, 3.2, and 7.0 % Sn composition grown in a commercially available CVD reactor. The temperature dependent spectral response, I-V curves, DC responsivity, and AC responsivity were measured from 300 to 77 K in 20 K increments. The temperature dependent spectral response measures the blue-shifting detector cut-off for each decreasing temperature due to the increasing bandgap. The electrical transport characteristics, extracted from the dark I-V curves, show decreasing carrier activation energy with increasing Sn mole fraction. The different sources of noise current within the material are evaluated based on these measurements. The measured AC responsivity and shot noise limited noise current were then used to calculate the predicted temperature dependent specific detectivity (D*) at 1.55 μm. The performance evaluations studied here provide the baseline performance for a cost effective $Ge_{1-x}Sn_x$ FPA integrated on Si for detection in the SWIR band.

2. Photoconductor fabrication

The photoconductor samples were grown in an ASM Epsilon® reduced pressure chemical vapor deposition reactor. A Ge buffer was first deposited on the Si substrate, annealed then the $Ge_{1-x}Sn_x$ epilayer was deposited immediately after within the same chamber. The $Ge_{1-x}Sn_x$ deposition process was kept below 450 °C. The epilayer thicknesses were measured using cross section transmission electron microscopy (TEM). The Sn compositions were measured using secondary ion mass spectrometry and were verified with x-ray diffraction (XRD) measurements of the lattice constants. Each sample was grown unintentionally doped, but Hall measurements showed that the 0.9, 3.2, and 7.0 had a p-type background carrier concentration of 2×10^{17}, 5×10^{17}, and 2×10^{17} cm^{-3}, respectively. Additionally, the Hall mobilities for these $Ge_{1-x}Sn_x$ layers ranged from 280 to 310 cm^2/(V·s). A summary of the $Ge_{1-x}Sn_x$ compositions and layer thicknesses of each sample in this study is presented in Table I. The level of strain in each sample (%) listed in Table 1 was directly determined from the XRD rocking curve scans and elastic (Poisson) ratio [15]. These rocking curve scans directly determined the out of plane lattice constant allowing the strain to be calculated. We define 100 % strain for films where the in plane lattice constant matches that of the Ge buffer and 0 % strain when the in plane lattice constant equals the out of plane lattice constant.

Table 1. Sn Composition and Thickness for Each Epilayer

Sn %	$Ge_{1-x}Sn_x$ Thickness (nm)	Ge Buffer Thickness (nm)	Strain (%)	FWHM from XRD Rocking Curve (°)
0.9	327	763	85	

3.2	76	684	84	0.20
7.0	240	755	49	0.34

The Ge buffer layers were intentionally grown relaxed to allow the Si/Ge dislocations to be confined at the substrate interface. The $Ge_{1-x}Sn_x$ layers were grown partially compressive strained on this relaxed Ge virtual substrate. The cross sectional TEM image of the sample with 3.2 % Sn in Fig. 1(a) shows the reduced number of defect sites at the $Ge_{1-x}Sn_x$/Ge interface compared to the Ge/Si growth interface. Further analysis using XRD was conducted on each sample to confirm the growth structures and crystallinity. The lower angle diffraction peaks in Fig. 1(b) are assigned to the $Ge_{1-x}Sn_x$ epilayers of each sample due to their larger out of plane lattice constant. The diffraction peak due to the 0.9 % Sn sample shows up as a shoulder on the Ge buffer peak and does not allow a FWHM determination. The 3.2 and 7.0 % Sn diffraction peaks are identifiable as separate peaks and the calculated FWHM are presented in Table 1. The average FWHM of the Ge buffer layer alone was measured to be 0.15 °. The samples studied here are analyzed for their bulk properties and were not optimized for detection performance. It is expected that further device improvements will be possible with an enhanced design.
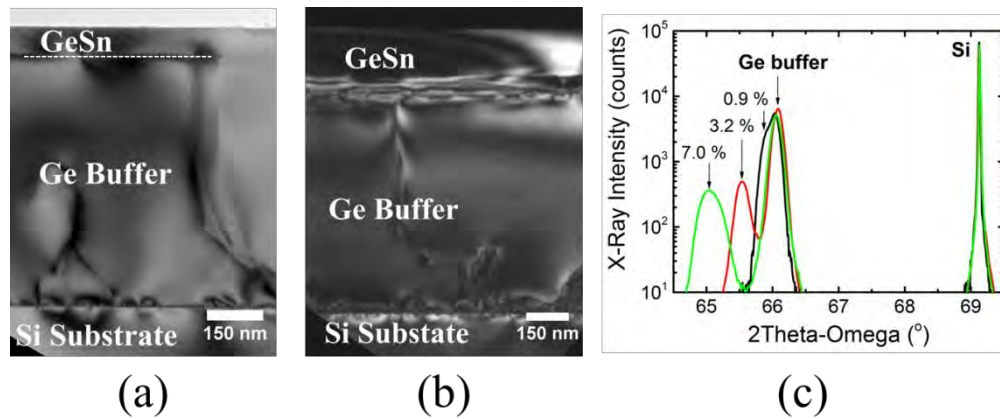

Fig. 1. Cross sectional TEM image of the (a) 3.2 % and (b) 7.0 % Sn sample shows the relaxed Ge buffer layer and strained GeSn layer with limited propagating defects. (c) The 2θ-ω XRD scan for each sample measures the increasing lattice constants with increasing Sn composition indicated by the lower diffraction angle.

The photoconductor fabrication was carried out using standard optical photolithography techniques to define the $Ge_{1-x}Sn_x$ mesas and deposit the metal contacts. The mesas were defined using a positive photoresist, then dry etched using a reactive ion etching (RIE) process with a CF_4 precursor. The photoresist was removed using a commercial resist stripper, then rinsed in DI water. Following this resist removal, the samples were loaded into a plasma enhanced chemical vapor deposition (PECVD) reactor for a thick 1300 nm SiO_2 deposition. Windows in the SiO_2 were opened up for the metal contacts using a buffered oxide etch. Immediately following this oxide etch, 10 nm of Cr followed by 200 nm of Au was deposited for the Ohmic contacts. These contacts showed a linear I-V behavior, thus no annealing was needed. A schematic cross section of the final device structure is shown in Fig. 2(a) and the top view optical image of the final fabricated photoconductor structure in Fig. 2(b) shows the co-planar design.
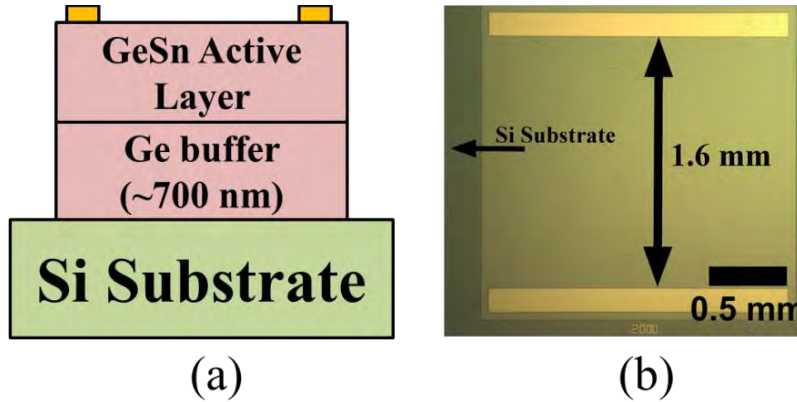
Fig. 2. (a) Cross section view of the growth structure and (b) top view optical image of the GeSn photoconductor shows a top contact, co-planar design.

3. Testing and measurement setup

The low temperature device testing was conducted within a Janis cryostat using liquid nitrogen cooling and a closed-loop temperature controller. Electrical connection to the photoconductor contacts was made via Ni tip probes going to an electrically isolated BNC feed through. The electrical characterization and DC bias conditions were measured with a Keithley 236 source-measure unit (SMU). The spectral response measurements were made using a Fourier transform infrared spectrometer. The white light from the internal tungsten source was externally focused and normally incident onto the entire sample active area upon exit of the interferometer. This method allows for full IR spectrum analysis without any high order diffraction ambiguity. However, this method precludes radiant flux calibrations of the intensity per wavelength. As a result the responsivity performance of these devices was measured using a laser diode with a 1.55 μm wavelength. The optical power of the laser diode was measured at the sample position using an ILX Lightwave power meter and the absolute responsivity values were verified using a NIST traceable InGaAs p-i-n photodiode. The dark and laser illuminated I-V curves, measured by the SMU, were used to determine the DC responsivity for the devices.

The specific detectivity (D^*) was calculated from the AC responsivity and device dark current under the equivalent electronic conditions. The D^* value is measured here since it is a key detector figure of merit for FPA design due to the inclusion of the device noise and normalized for device area. The AC responsivity was measured by optically chopping the incident light at 345 Hz and measuring the photoresponse output using a lock-in amplifier. This chopping frequency was chosen to allow sufficient suppression of 1/f noise. To limit the equivalent noise bandwidth (ENBW) to the standard 1 Hz, the time constant and slope/oct were appropriately set on the lock-in amplifier to 100 ms and 18 dB/oct, respectively. The modulated voltage response was measured by the lock-in amplifier across a 50 Ω load resistor in series with the photoconductor device, and the current response was calculated from this load. The dark current measurement under same electronic conditions was used to calculate the noise current. The final D^* value is calculated using the relationship, $D^* = R_{AC} \times \sqrt{A}/I_{noise}$ where R_{AC} is the AC responsivity, A is the device area, and I_{noise} is the calculated noise current.

4. Temperature dependent characterization

4.1 Electrical characterization

Electrical characterization of each sample was performed from 300 to 77 K. The dark resistance values shown in Fig. 3 were extracted from the dark I-V curves at each temperature.

Dark I-V data for sample of 0.9 % Sn is shown in Fig. 3 (inset) as a representative data set for the 3.2 and 7.0 % Sn samples. The linear dark current relationship versus the applied voltage indicates that good Ohmic contacts were made. The dark resistance for each photoconductor is increasing with decreasing temperature. This increase in dark resistance for decreasing temperature is due to the decreasing number of activated carriers in the device. Three distinct regions were observed across the temperature measurement range on all the samples. Region 1 marks the carrier freeze out region. Region 2 is the extrinsic region where carrier ionization is complete, but carrier generation still occurs due to lower energy trap and defect states. Region 3 is the intrinsic region where at higher temperatures carriers are thermally excited across the bandgap leaving a material with equal electron (n) and hole (p) concentrations. As the temperature decreases the overall performance of these devices will increase due to the decreased number of thermally activated carriers resulting in a lower dark current and lower noise current.
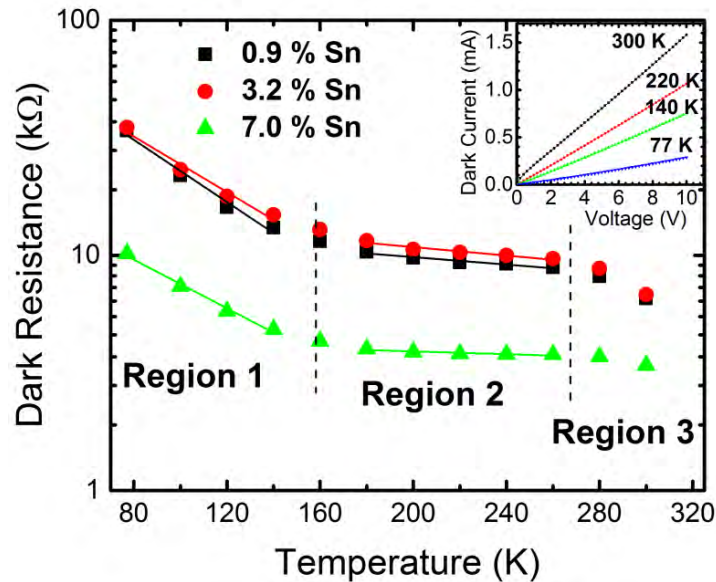

Fig. 3. Dark resistances for each sample are extracted from the I-V measurements and plotted at the measured temperature. The three distinct temperature regions for all samples marked as Regions 1 – 3 are the carrier freeze out, trap activated, and intrinsic regions, respectively. (Inset) I-V measurement of the 0.9 % Sn sample shows the linear behavior expected for photoconductive device.

4.2 Optical characterization

The temperature dependent spectral response measured for each $Ge_{1-x}Sn_x$ photoconductor is shown in Fig. 4. Only the intermediate temperature dependent response measurements are shown here for clarity. The spectral response in Fig. 4(a) directly compares the increased long wavelength behavior between the 0.9 and 3.2 % Sn samples. The absorption edge of the 0.9 % Sn sample shows a red-shift of the direct Γ-valley absorption edge beyond that of Ge for the 300 K measurement indicated by the response cut-off beyond 1.6 μm. The dominant Γ-valley absorption edge for the 3.2 % Sn sample, which has a thinner $Ge_{0.968}Sn_{0.032}$ active layer, is attributed to the underlying Ge buffer, while the weaker extended response out to 1.9 μm is due to the indirect L-valley absorption of the $Ge_{0.968}Sn_{0.032}$ layer. The spectral response of the 7.0 % Sn sample in Fig. 4(b) shows an extended response beyond 2.1 μm at high temperatures and a cut-off that is still beyond 1.9 μm at 77 K. It is expected that spectral response of this detector is further extended beyond 2.1 μm; however, the spectral response signals at temperatures above 260 K for this sample were too noisy to be considered valid. The signal

distortion in Fig. 4(b) from 1.8 to 1.92 μm is due to atmospheric absorption and appears in all measurements regardless of sample temperature.
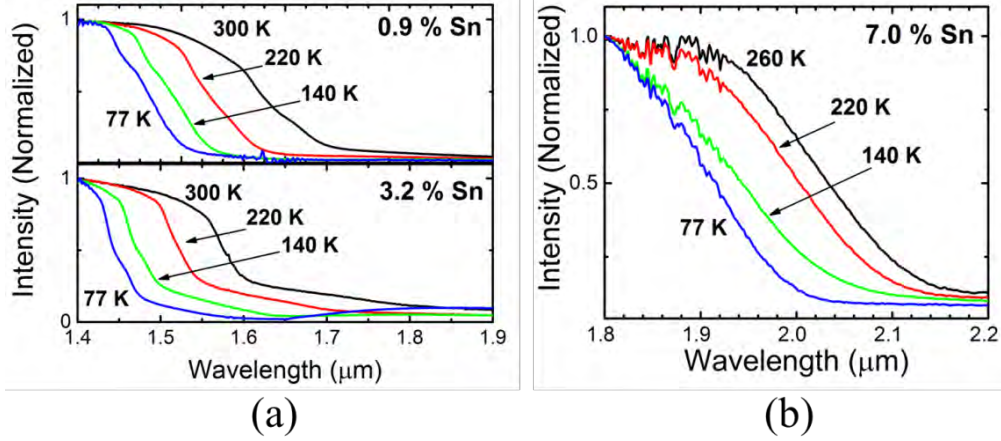

Fig. 4. Normalized spectral response of the (a) 0.9, 3.2 , and (b) 7.0 % Sn photoconductors for different temperatures as a function of wavelength shows the shifting absorption edge for increased Sn composition.

The temperature dependent cut-off wavelength for each sample designates the approximate absorption band edge. The Vegard's law interpolation of the shifting bandgap as a function of Sn composition is well documented at 300 K [26]. Here we study the temperature dependent bandgap for each composition described by the Varshni relationship, $E(T) = E(0) - (\alpha \times T^2)/(\beta + T)$ where E(0) is the bandgap at 0 K, T is absolute temperature, and α and β are fitting parameters. The long wavelength 50 % cut-off for each detector was extracted from the temperature dependent spectral response measurements [27-30]. To distinguish between an indirect and direct absorption edge, we relate the bandgap dependent absorption coefficient to the measured photoresponse using the classical relationship for a photoresponse current, I_{arb},

$$I_{arb} = \eta_i q\lambda/(hc) \cdot (1 - R_\lambda) \cdot P_\lambda \cdot (1 - \exp(-\alpha_\lambda w)) \tag{1}$$

where η_i is the internal quantum efficiency, λ the wavelength, R_λ the surface reflectivity, P_λ the spectral power incident on the device, α_λ is the absorption coefficient and w is the device thickness. The spectral output of the tungsten white light source was measured to be linear across this wavelength band using the calibrated InGaAs photodiode, thus the spectral dependence can be ignored. Additionally, the thick SiO_2 passivation layer is large enough to reject non-band structure related inferences. The remaining spectral dependent component is the band dependent absorption coefficient. For the case when the thickness is much smaller than the skin depth, $\alpha_\lambda w \ll 1$, then Eq. (1) reduces to,

$$I_{arb} = C (-\alpha_\lambda) \tag{2}$$

where C is a constant independent of wavelength. The strong spectral dependence of the absorption coefficient due to the electronic band structure of the material allows for distinction between direct and indirect absorption based on the photoresponse curve [31]. Finally, the distinction between direct and indirect transitions becomes apparent through examination and fitting of the energy depedent absorption coefficient [32],

$$\alpha \propto \left[h\nu - E_g\right]^m \tag{3}$$

where E_g is the bandgap, hν is the photon energy, and m is a constant. Here the constant, m, equals 2 for allowed indirect transitions and 1/2 for allowed direct transitions. The data for the

7 % Sn sample at 77 K measurement was fitted using Eq. 3 at the different absorption edges as marked in Fig. 5. In this figure, the region from 1.5 to 1.6 μm is attributed to the direct bandgap of Ge buffer, confirmed by the fitted power equal to 0.51. The long wavelength absorption edges beyond 2.1 μm is due to the indirect $Ge_{0.93}Sn_{0.07}$ valley with $m = 2.03$. The middle absorption marked by a fitted $m = 1.01$ is less clear and is likely an overlap of the $Ge_{0.93}Sn_{0.07}$ direct and Ge buffer indirect absorption. The lack of direct gap absorption for this partially strained-layer sample indicates that the indirect-to-direct crossover does not occur at 7.0 % Sn. Since we do not observe an additional high slope absorption edge at extended wavelengths for the $Ge_{1-x}Sn_x$ alloy, then we conclude that this material has an indirect bandgap. In comparison, the direct gap transition for a 9 % Sn sample was observed by extrapolation of a photoconductor spectral response at 100 K [33].
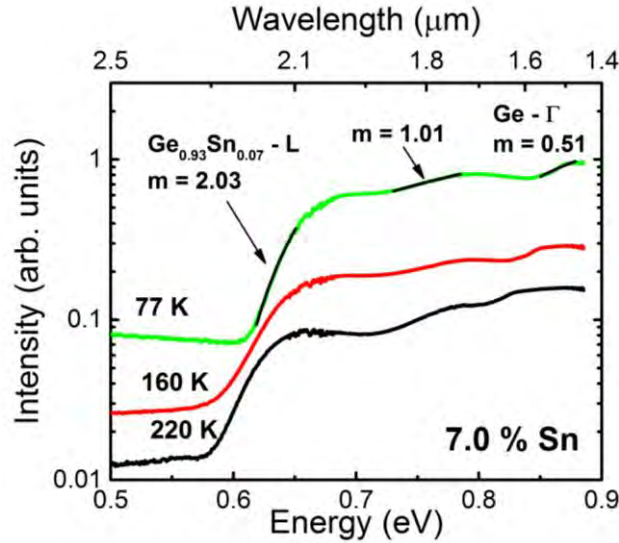

Fig. 5. Absolute spectral response temperature profile of the 7.0 % Sn photoconductor shows increasing response intensity for decreased temperature. The absorption edge slope indicates either direct or indirect absorption.

The long wavelength 50 % cut-off of each sample and absorption edge, plotted in Fig. 6, was fitted as a function of temperature using the Varshni relationship. For comparison, the Ge direct band has been also been plotted [34]. The disappearance of a measurable indirect absorption edge for the 3.2 % Sn sample, at decreased temperatures, prevented a fit for this sample. The reduced indirect absorption edge for this 3.2 % Sn sample becomes dominated by the indirect absorption of the much thicker Ge buffer layer, reducing the ability to distinguish the two. Additionally, the high noise for the 7.0 % Sn at increased temperatures above 260 K reduced the signal quality, precluding those data points to be included in the fitting. The fitted parameters for the 0.9 and 7.0 % Sn photoconductors presented in Table 2 shows the expected trend of decreasing E(0) for increasing Sn composition.
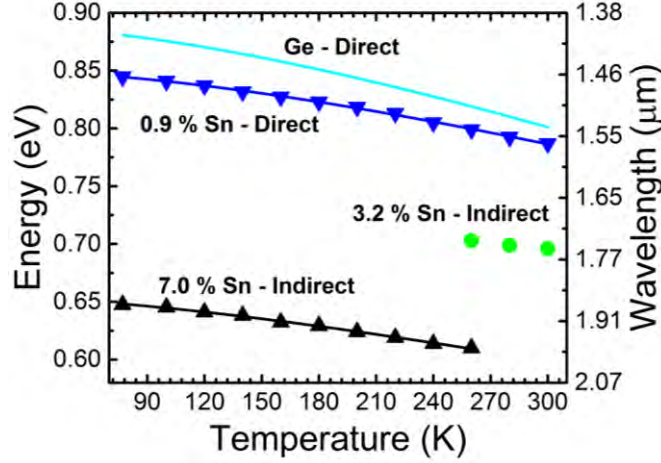
Fig. 6. The extracted absorption edge cut-off wavelengths for the 0.9, 3.2, 7.0 % Sn, and the calculated Ge direct [34] are plotted for each temperature. The temperature dependent Varshni relationship fit line is drawn across the 0.9 and 7.0 % Sn data sets.

Table 2. Temperature Dependent Parameters Fitted for the Varshni Relationship

Fitting Parameters	Ge - E_Γ [34]	0.9 % Sn – E_Γ	7.0 % Sn – E_L
E(0) (eV)	0.889	0.851	0.654
α (eV/K)	6.8×10^{-4}	5.1×10^{-4}	3.5×10^{-4}
β (K)	398	416	269

The DC responsivity values at 1.55 μm were obtained by measuring the change in current due to the normal incident laser with a 1.2 mW optical power. The dark and laser illuminated I-V curves measured for each temperature were used to calculate the responsivity value at each temperature vs the bias voltage, shown in Fig. 7. For clarity, the responsivity values reported in Fig. 7 show only four temperatures for each sample. At decreased temperatures, the overall response is expected to increase due to the decreased number of thermally active carriers, but for the 0.9 and 3.2 % Sn samples, the maximum responsivity occurred at 140 K. This is a result of the dominant absorption edge for both of these samples near 1.55 μm, blue-shifting with decreasing temperature, which is due to the increasing bandgap with decreasing temperature. Alternatively, the lower bandgap and increased density of states for the 7 % Sn sample shows a trend of monotonically increasing responsivity at 1.55 μm for decreasing temperature. The maximum responsivity measured for the 7.0 % Sn sample at 77 K was 0.179 A/W. This is a substantial increase above the responsivity measurement at 300 K, which was around the lower limit of our system at 0.0005 A/W. The linear increase in responsivity vs applied voltage bias for these devices is indicative of the photoconductive gain, defined as the ratio of the carrier lifetime to the transit time, $G = \tau_l/\tau_n$ [35]. The photoresponse in these devices is described by, $I_{photo} = \Delta\sigma \cdot A/L \cdot V$ where A is the area, L is the length, V is the applied voltage bias, and $\Delta\sigma$ is the change in conductivity due to the incident light. The change in conductivity under steady state is $\Delta\sigma = q(\mu_n + \mu_p)G_o\tau_n$ where q is the elementary charge, G_o the generation rate, τ_n the transit time, and μ_n, μ_p are the electron and hole mobilities, respectively. The proportionate relationship for the mobility, device length, and transit time would allow for a further increase in device performance for a reduced length between metal contacts, as well as for materials with reduced scattering and higher mobilities.
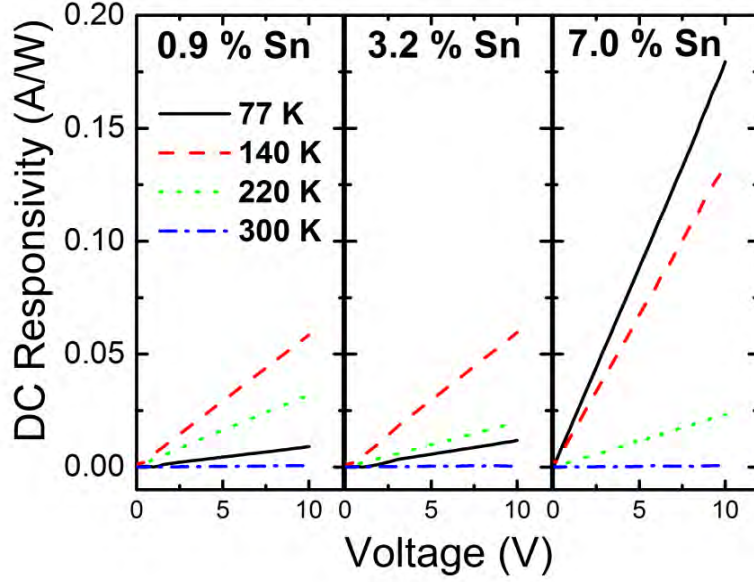
Fig. 7. The DC responsivity values for a 0.9, 3.2, and 7.0 % Sn photoconductor extracted from both the dark and illuminated I-V measurements. The illuminated condition is a 1.55 μm diode laser with 1.2 mW optical power.

5. Discussion

5.1 Noise analysis

The dominant electronic noise current within a photoconductor is due to thermal fluctuations (Johnson-Nyquist), generation-recombination (G-R) of carriers, and shot noise. Photoconductors have generally higher dark currents than photodiodes. Thus, these devices are not expected to have a significant source of 1/f noise for non-DC measurement conditions above 1 Hz [36]. Excluding 1/f noise, the total noise current is described by: $I_{noise} = \sqrt{I_{thermal}^2 + I_{G-R}^2 + I_{shot}^2}$. The Johnson-Nyquist noise depends on the thermal fluctuations of carriers within the material calculated by, $I_{thermal} = \sqrt{4kT(BW/R)}$ where k is Boltzmann constant, T is absolute temperature, BW is the electronic bandwidth, and R is the resistance. Shot and G-R noise sources are directly related to the dark current and are described by, $I_{shot} = \sqrt{2qI_{dk}(BW)}$ and $I_{G-R} = \sqrt{4qI_{dk}(BW)}$ where q is the electron charge and I_{dk} is the dark current. The measurement bandwidth is commonly conducted with 1 Hz equivalent noise bandwidth (ENBW) thus allowing comparable noise measurements between devices. Based on the measured dark current and resistance of these devices at each temperature, the calculated noise current is dominated by the high dark current with negligible contribution from Johnson-Nyquist mechanism. Thus, this thermal noise component can be ignored.

Both shot and G-R noise are current dependent, but the dominant source of G-R noise is trap and defect sites, creating greater fluctuations in the carrier density throughout the photoconductor. To better identify the G-R noise contributions in this material, the detector design was focused on the elimination of other significant recombination mechanisms. The co-planar design of these devices allows for the G-R noise due to heterojunction transitions to be minimized. This reduces transitions among different energy bands at the heterojunction interface. These heterojunction boundaries create an added G-R zone due to the discontinuity of electron density and varying mobilities between layers [37]. Additional recombination centers at the surface were minimized through the deposition of a thick 1300 nm SiO_2 layer onto the devices following mesa etching. The use of SiO_2 as the passivation layer was chosen since it is a widely available material used in all Si CMOS fabrication facilities. Material

specific G-R mechanisms are: radiative recombination, Auger recombination, and Shockley-Read Hall (SRH) process. Each has a recombination rate with a different dependency on the carrier concentration levels (n). Radiative and Auger recombination have recombination rates that follow $\sim n^2$ and n^3 relationships [38], while SRH process has a linear relationship with n. This study isolates the carrier activation energy related to the SRH process.

The dark resistance of each device measured for varying temperatures allows the extraction of the carrier activation energies. The measured resistance of the photoconductors is related to the conductivity (σ) by: $R = l/(A \times \sigma)$. Additionally, the dark conductivity is described by $\sigma = q \times (n\mu_n + p\mu_p)$. The temperature dependent conductivity for a semiconductor is dominated by the change in carrier concentration, hence a general Arrhenius relationship for conductivity can be derived, $\sigma = C_1 \exp(-E_A/(2kT))$ [32]. The measured resistance can then be related to the activation energy for the majority carriers with the expression,

$$R = C_2 \exp\left(\frac{E_A}{2kT}\right) \tag{4}$$

where E_A is the activation energy, k is the Boltzmann constant, and C_1, C_2 are constants. The carrier activation energy, E_A, was extracted from the slope of the Arrhenius plot shown in Fig. 8 (a) based on Eq. (4). The extracted values from Fig. 8(a) give the activation energy of the ionized carrier states (Region 1), and the surface/defect activation energies (Region 2). The surface/defect states give rise to the generation-recombination noise and should be suppressed by passivation or annealing in future generation devices. For both regions, there is a general trend of decreasing activation energies for increasing Sn composition shown in Fig. 8(b). It is well documented that for both Ge and low Sn composition $Ge_{1-x}Sn_x$, the defects are acceptor type [39-41]. This decrease in activation energy for increasing Sn mole fraction can be explained by acceptor type defect sites being neutralized with donor level states from Sn atoms.
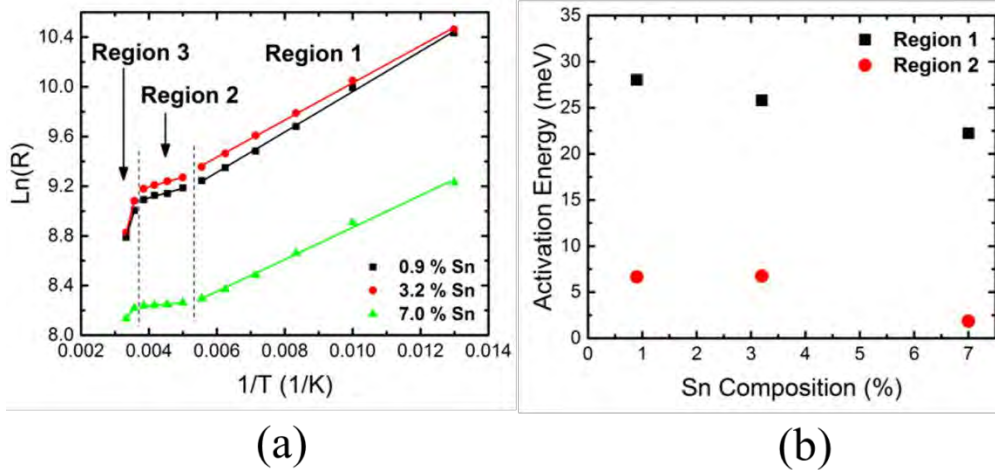

Fig. 8. (a) The Arrhenius plot of Ln (R) vs 1/T plot is linearly fitted for Regions 1 and 2 for from the DC I-V data. (b) The extracted activation energies are shown for each 0.9, 3.2, and 7.0 % Sn photoconductor.

5.2 Specific detectivity (D^*)

The notable presence of defect sites and high carrier concentrations indicate the dominant noise mechanism can be approximated from the dark current as described earlier. The calculated noise current and measured AC responsivity at 345 Hz with a 1 Hz ENBW allow D^* to be determined at the illuminated wavelength of 1.55 μm. The maximum D^* values for each sample are presented in Fig. 9. The low Sn composition samples [Figs. 9(a) and 9(b)]

show a peak D^* at temperatures above 77 K for the same reason as explained previously for the DC responsivity. However, for these two samples the maximum D^* occurs at different temperatures than for the maximum DC responsivity due to the differing levels of dark current and AC responsivity between these detectors. The higher Sn composition sample in Fig. 9(c) shows an increasing D^* for decreasing temperature, with a maximum measured value of 1×10^9 cm·√Hz/W at 77 K. The reduced carrier concentration and noise components are not competing with the blue shifting absorption band edge in this 7.0 % Sn sample. Therefore, the overall increasing AC responsivity for this sample allows for the unambiguous baseline for D^* of this photoconductor. In future work, the Sn content could be increased well above 7 % which would reduce the (direct) E(0) bandgap considerably. Thus, but selecting the $Ge_{1-x}Sn_x$ composition, the wavelength at which peak D^* occurs could be engineered to be within the range from 2 to 20 μm. Further improvements in the D^* for this material are expected for p-i-n photodiode designs with $Ge_{1-x}Sn_x$ active regions, which will further reduce the dark current and decrease the noise current.
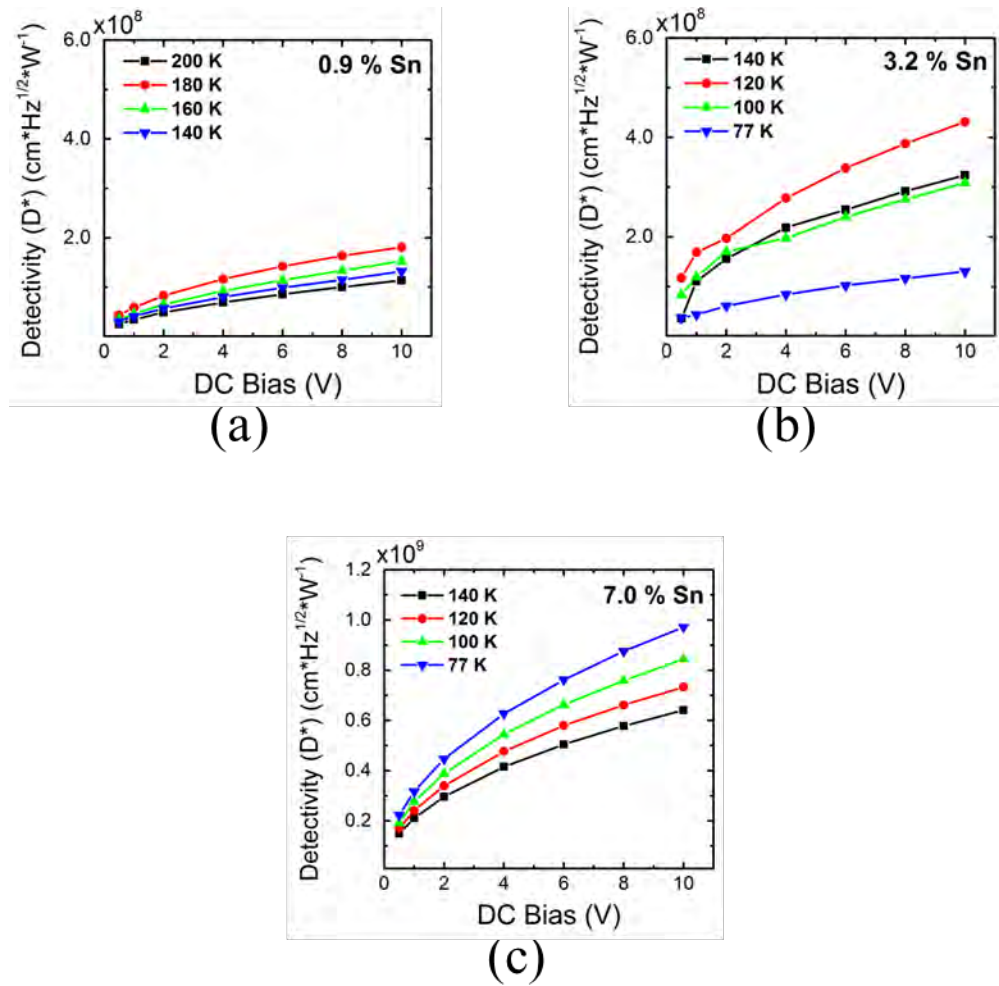

Fig. 9. Temperature dependent specific detectivity (D^*) for the (a) 0.9 , (b) 3.2, and (c) 7.0 % Sn samples were calculated from the measured AC responsivity and calculated noise current.

From a supply chain perspective, the growth of these materials in a commercially available and CMOS compatible CVD reactor will allow for a faster commercialization.

Direct incorporation of a SWIR FPA in a CMOS process not only reduces cost and increase array size, but it also adds readout architecture functionality. This incorporation provides the use of current CMOS sensor architectures as either active pixel sensor (APS) or passive pixel sensor (PPS). The APS is a design that uses a switch and amplification per pixel for low noise voltage amplification, while PPS is a simple switch and pixel design that allows for a higher optical fill factor and lower processing cost. Thus, multispectral imaging can be achieved by using variable Sn mole fraction detectors. These pixels can then be appropriately matched for optimal low noise amplification, or higher optical absorption through this CMOS processing.

6. Conclusion

The temperature dependent spectral response of 0.9, 3.2 and 7.0 % Sn photoconductors were measured from 300 to 77 K. The observed blue-shifting cut-off with decreasing temperature allowed the temperature dependent Varshni relationship to be fitted. The DC responsivity of these devices was also characterized for different temperatures at 1.55 μm wavelength. The measured dark resistance as a function of temperature exhibited separate carrier activation energies for each Sn composition. The activation energy of the ionized accepter and trap states showed a decreasing trend of activation energy for increasing Sn composition. Future studies and device architectures are needed to identify suppression mechanism for these sites in order to reduce the overall noise current. A baseline specific detectivity (D^*) values was determined for each sample, and a maximum 1×10^9 cm·$\sqrt{Hz}$/W was measured for the 7.0 % Sn photoconductor. The performance of these simple structures indicates a promising future for $Ge_{1-x}Sn_x$ photodetectors. The crystalline growth of these samples in a commercially available CVD reactor, compatible with Si CMOS process, allows for these infrared detectors to be available for immediate commercial implementation.